Supporting Information

On-site decoking of Ca-looping process achieves 1000 cycles of stable thermochemical energy storage

Han Li,[ab‡] Ke Tang,[ab‡] Jiashun Wang,[ab‡] Jinfeng Lin,[ab] Xianfeng Qiao,[ab] Junwei Li,[c] Hangbin Zheng,[ab] Yan Zhuang,[ab] Zhengxin Ding,*[ab], Mingkai Fu,*[d] Pengzhao Wang,[e] Jinjia Wei [f] and Jinlin Long *[ab]

a. State Key Laboratory of Chemistry for NBC Hazards Protection, College of Chemistry, Fuzhou University, Fuzhou 350116, P. R. China.

b. State Key Laboratory of Photocatalysis on Energy and Environment, College of Chemistry, Fuzhou University, Fuzhou 350116, P. R. China.

c. Department of Chemical Engineering, KU Leuven, Celestijnenlaan 200F, B-3001 Leuven, Belgium.

d. Institute of Electrical Engineering, Chinese Academy of Sciences, Beijing, 100190, China.

e. College of Chemical Engineering, Fuzhou University, Fuzhou 350108, P. R. China.

f. School of Chemical Engineering and Technology, Xi'an Jiaotong University, Xi'an, Shaanxi 710049, China.

* Corresponding Author. E-mail: zxding@fzu.edu.cn; fumingkai@mail.iee.ac.cn; jllong@fzu.edu.cn

‡ These authors contributed equally to this work

Materials and Methods

Chemicals

Calcium nitrate tetrahydrate (98%, $Ca(NO_3)_2 \cdot 4H_2O$), aluminum nitrate nonahydrate (99%, $Al(NO_3)_3 \cdot 9H_2O$), cerium nitrate hexahydrate (99%, $Ce(NO_3)_3 \cdot 6H_2O$), citric acid monohydrate (98%, $C_6H_8O_7 \cdot H_2O$) ,and Ethylene glycol (98%, $(CH_2OH)_2$) are obtained from Shanghai Sinopharm Chemical Reagent Co., Ltd. Manganese nitrate solution (50%, $Mn(NO_3)_2$) and carbon black are purchased from Shanghai Aladdin Biochemical Technology Co., Ltd. All the chemical reagents in this work are of analytically pure grade, and used directly without further purification.

Synthesis protocol for metal-doped CaO-looping materials

The Al/Mn/Ce Co-doped CaO nanomaterials are synthesized via an improved sol-gel method. Firstly, the 2.3616 g of calcium precursor ($Ca(NO_3)_2$ $4H_2O$) and doping material precursor ($Al(NO_3)_3$ $9H_2O$, $Ce(NO_3)_3$ $6H_2O$, 50wt% $Mn(NO_3)_2$ solution, the amount of doped material precursors is in proportion to the Ca atoms) are dissolved into distilled water. Subsequently, citric acid monohydrate is added to the precursor solution slowly with a mixer stirring. The molar ratio of calcium ion to distilled water to citric acid is maintained at 1:100:1.5. Next, the mixed solution is stirred for 30 min first and agitated at a temperature of 80 ℃ for 2.5 h to obtain a uniform sol. The wet sol is transferred into an oven drying and foaming at 110 ℃ for 6 h, and it is then combusted for 1 h in a muffle furnace heated to 300 ℃ with a heating rate of 10 ℃ min^{-1}. The intermediate material is fully ground into a fine powder both after drying and after combusting. Finally, the powder is calcined in the muffle furnace at 800 ℃ for 2h with the same heating rate to obtain the Al/Mn/Ce co-doped CaO nanomaterials.

During the calcination step, a great number of pores will be generated under the decomposition of citric acid and nitrate to increase the specific surface area. Moreover, carbonization of citric acid followed by removal of the carbon template reduces the grain size of the as-result solids. By two-step sufficient grinding, the phase formation between calcium element and doped elements is more uniform under high temperature, and the anti-sintering abilities of the Al/Mn/Ce co-doped CaO materials are expected to be strengthened.

Following the previous progress, the Al/Mn/Ce co-doped CaO materials with mole ratios of Ca: Al: Mn: Ce = 100:4:4:2, 100:8:8:4, 100:10:10:5 are prepared, and denoted as Ca|4Al-4Mn-2Ce, Ca|8Al-8Mn-4Ce, Ca|10Al-10Mn-5Ce, respectively. Further, Ca|5Al-5Mn is synthesized to research the effect of Ce lattice doping based on the Al/Mn doping. The pure CaO is also prepared using a similar procedure as a reference and it is denoted as CaCA. In addition, Ca|5Al-5Mn-5Ce, Ca|8Al-5Mn-5Ce, Ca|12Al-5Mn-5Ce, Ca|5Al-8Mn-5Ce, Ca|5Al-12Mn-5Ce, Ca|5Al-5Mn-8Ce and Ca|5Al-5Mn-2Ce are prepared to explore the effect of changing the single-component doping content on the energy storage performance of CaO under Al/Mn/Ce co-doping conditions.

Characterizations

The micromorphology of all samples is observed by field emission scanning electron microscopy (FESEM, Hitachi SU-8000). Besides, transmission electron microscopy (TEM, Tecnai G2 F20, FEI Company, USA) and high-resolution transmission electron microscopy (HRTEM, Tecnai G2 F20, FEI Company, USA) are also used to characterize the morphology and microstructure of the as-prepared nanomaterials.

X-ray photoelectron spectroscopy is carried out on a Thermo Fisher Scientific K-Alpha XPS system with a monochromatized Al K alph X-ray source (test tube voltage: 15kV, test energy: 1486.8eV). According to the chemical reaction ($4Ce^{4+} + O^{2-} \rightarrow 4Ce^{4+} + 0.5O_2 + 2e^-/\square \rightarrow 2Ce^{3+} + 2Ce^{4+} + 0.5O_2 + \square$), the surface oxygen vacancies (denoted as □) in Ce-doped CaO samples are intimately associated with the surface Ce^{3+} concentration that iss quantified by a semiquantitative method of integrated peak areas (S) from the eq. 1 below[1]. As listed in Table S4, see supporting information.

$$C_{\square} = \frac{1}{2}C_{Ce^{3+}}(\%) = \frac{S_{u^0} + S_{u'} + S_{v^0} + S_{v'}}{\sum S_u + S_v} \text{x}100\% \quad \text{(eq. 1)}$$

A N_2 physical adsorption analyzer (Micromeritics 3Flex) is used to measure the pore size distribution of the energy carriers, and the specific surface area and pore volume are calculated by the Brunauer-Emmett-Teller (BET) method and Barrett-Joyner-Halenda (BJH) model,

respectively.

X-Ray diffraction is carried out on a Bruker D8 Advance X-ray diffractometer, and the scanning size was set at 0.013° with the scan range 5°- 80°. The CaO crystallite size is determined from Debye-Scherrer's equation in eq.2:

$$D = \frac{0.89 \times \lambda}{\beta cos\theta}$$

(eq.2)

where D is addressed to the average grain size, λ is the length of radiation wave (Copper-Kα, λ =1.5406 Å), β corresponds to the full width at half maximum, and θ represents the Bragg angle of the peak.

The spectral reflectance ($R(\lambda)$) of samples is measured on a Varian Cary 500 Scan UV-Vis-NIS spectrophotometer using $BaSO_4$ as a reference, ranging from 300 to 2500 nm. Moreover, UV-Vis DRS spectra are also measured by a Varian Cary 500 Scan UV-Vis-NIS spectrophotometer, ranging from 200 to 2500 nm (according to the solar spectrum energy distribution). To quantitatively evaluate the solar absorption capability of the different samples, the average solar absorptance is defined as eq.3:

$$A_{ave} = \frac{\int_{300nm}^{2500nm} \alpha(\lambda) I(\lambda) d\lambda}{\int_{300nm}^{2500nm} I(\lambda) d\lambda} \quad \text{(eq.3)}$$

where A_{ave} represents the average solar absorptance, λ is the wavelength, $\alpha(\lambda)$ stands for the spectral absorption and it can be calculated from the formula: $\alpha(\lambda) = 1 - R(\lambda)$, $I(\lambda)$ denotes the solar spectrum under AM1.5D conditions.

The Raman spectra of the materials are collected using a confocal Raman spectrometer (invia reflex, Renishaw company) and an Ar ion laser source (532 nm) within the range of 1000-3000 cm^{-1}. The electron paramagnetic resonance (EPR) spectra are measured using a Bruker ESP300E spectrometer equipped with a cylindrical cavity. The elemental analysis test is conducted at Unicube (in Germany, Elementar).

Cyclic thermal energy storage/release tests

To more comprehensively evaluate the cyclic stabilities and inactivation mechanism of samples, mid-term and long-term cyclic tests are carried out. The sample mass placed in the crucible is controlled between 6 and 7 mg in all experiments. Mid-term cyclic thermal energy storage tests (50 - 100 cycles) are measured using a thermogravimetric analyzer (TGA, Netzsch STA 449F4 Jupiter). In a single cycle, the sample is preheated to 800 ℃ for 10 min under a pure N_2 atmosphere (100 mL min^{-1}). Then the temperature is maintained at 800 ℃ to begin the calcination/carbonation cycle. The calcination process is performed at 800 ℃ for 6 min under a pure N_2 atmosphere (100 mL min^{-1}), and the carbonation process is conducted at 800 ℃ for 10 min under an 80% CO_2 atmosphere (20 mL min^{-1} N_2, 80 mL min^{-1} CO_2)

In addition, long-term cyclic tests (500 cycles) are conducted on a simultaneous thermal analyzer (STA, Linseis STA PT1600). The carbonation time is set to 7.5 min instead of 10 min. The other measurement conditions are set to be the same as described above.

Firstly, the Ca|10Al-10Mn-5Ce sample that has been cycled 500 times is tested for 501^{th} - 600^{th} cycles without oxygen to explore its stability during the coke accumulation process. Secondly, the pure N_2 introduced in the calcination step in the TG test is switched to an O_2/N_2 gas mixture with an oxygen content of 25vol% for 601^{th}-700^{th} cycle tests. The test conditions of the carbonation step remain to be unchanged. Finally, the gases in the calcination step and carbonation step in the TG test are switched to an O_2/N_2 gas mixture with an oxygen content of 25vol% and an O_2/CO_2 gas mixture with an oxygen content of 25vol%, respectively, for 701^{th}-800^{th} cycle test.

The CO_2 absorption capacity (C_N) and absorption rate (R_N) are calculated according to the following eq.4 and eq.5:

$$C_N = \frac{m_{car,N} - m_{cal,N}}{m_{cal,N}} \quad \text{(eq.4)}$$

$$R_N = \frac{dC_N^t}{dt} \quad \text{(eq.5)}$$

where N indicates the number of energy storage cycles, $m_{car,N}$ and $m_{cal,N}$ refer to the mass of samples after carbonation/calcination at cycle N, respectively. The effective conversion (X_N) and energy storage density (E_N) are the key parameters to evaluate energy storage performance of energy carriers, which are given by eq.6 and eq.7:

$$X_{CaO,N} = \frac{C_N}{f} \times \frac{M_{CaO}}{M_{CO_2}} \quad \text{(eq.6)}$$

$$E_N = \frac{C_N \times \Delta_r H_m^{\Theta}}{M_{CO_2}} \quad \text{(eq.7)}$$

where $\Delta_r H_m^{\Theta}$ is the standard reaction molar enthalpy of the carbonation reaction (178 kJ mol^{-1}), all existing literature adopts this reaction enthalpy, M_{CaO} represents molar mass of CaO, M_{CO_2} represents molar mass of CO_2, f refers to the mass fraction of CaO in the sample.

Density functional theory calculations

The DFT calculations are conducted on the Vienna Ab initio Simulation Package (VASP) code[2]. The interaction of core and electrons is treated by projector augmented wave (PAW) pseudopotential[3] with a cut-off energy of 520 eV. The exchange-correlation function is described by the generalized-gradient approximation-Perdew-Burke-Ernzerhof (GGA-PBE)[4]. A *ca.* 20 Å thick vacuum layer is used to eliminate the interaction between two adjacent slabs. Convergence in geometry optimization is reached when the force on each atom is below 0.02 eV Å^{-1}. The DFT-D3(BJ) method is used to consider the vdW-dispersion energy-correction[5]. The Brillouin zone is sampled on the Gamma-centered Monkhorst-Pack (MP) grids[6]. The data processing is assisted by VASPKIT[7] and VESTA[8] software.

A possible main contributor is the strong interfacial interaction between the Al/Mn/Ce-co-doped CaO-looping materials and adjacent CaO NPs, making the CaO migration more difficult. Therefore, we calculate a series of adsorption energies. The adsorption energy can be expressed as:

$$E_{ads} = E_{total} - E_{slab} - E_{adsorbent} \quad \text{(eq.8)}$$

Where E_{total} is the total system energy of the adsorbate on the material surface, $E_{adsorbent}$ is adsorbed energy and E_{slab} is surface energy[9].

The Gibbs free energy difference (ΔG) between initial and final states is denoted as:

$$\Delta G = \Delta E + \Delta ZPE - T\Delta S \quad \text{(eq.9)}$$

where E, ZPE, T and S represent the energy from DFT calculation, zero-point energy, temperature (1073.15 K) and entropy, respectively[10].

Figure S1 to 21

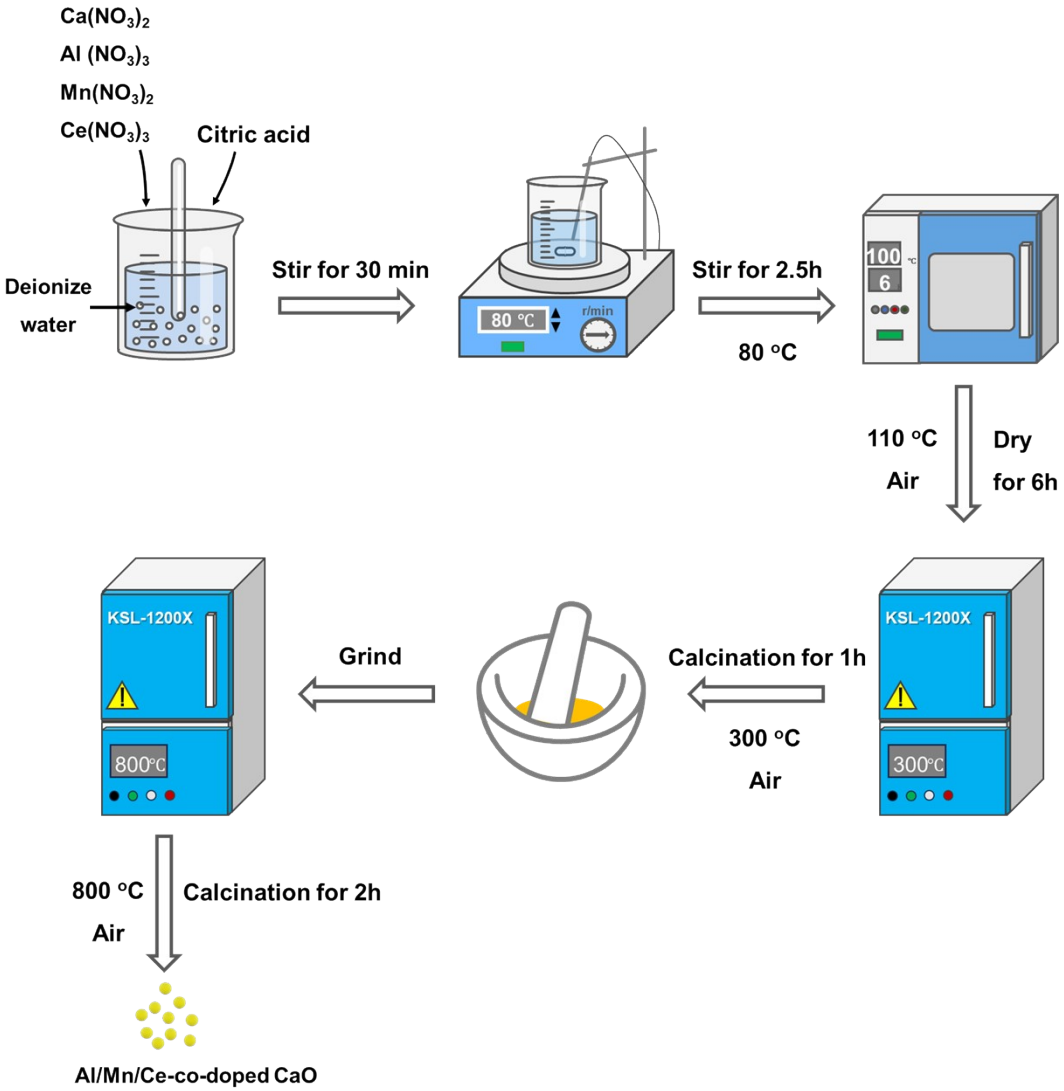

Figure S1. Preparation procedure of ternary component-doped CaO nanomaterials

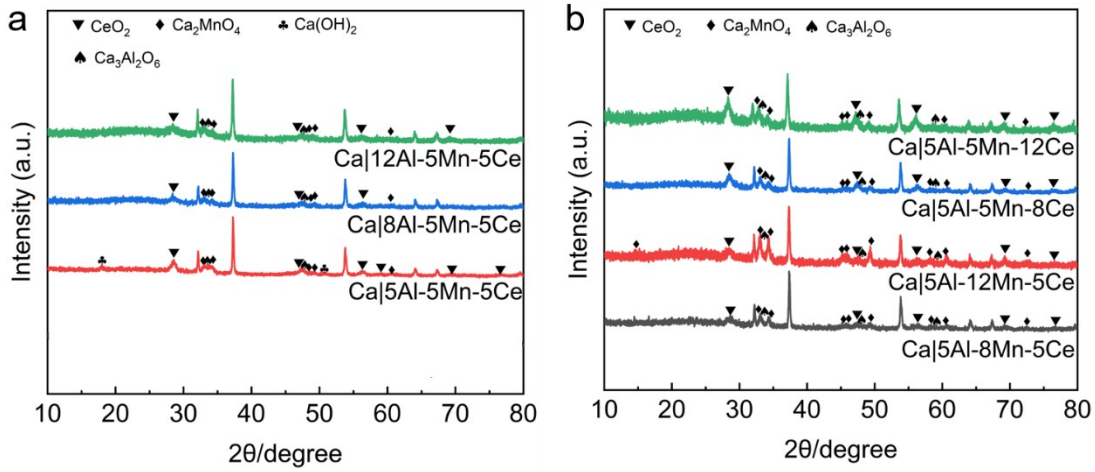

Figure S2. XRD pattern. (**a**) Ca|5Al-5Mn-5Ce, Ca|8Al-5Mn-5Ce, and Ca|12Al-5Mn-5Ce nanocarriers; (**b**) Ca|5Al-8Mn-5Ce, Ca|5Al-12Mn-5Ce, Ca|5Al-5Mn-8Ce, and Ca|5Al-5Mn-12Ce nanocarriers.

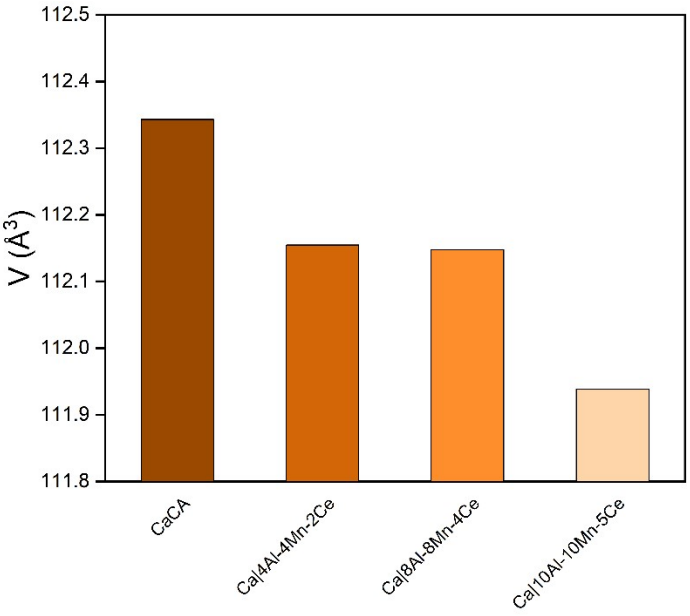

Figure S3. The cell volume of CaCA, Ca|4Al-4Mn-2Ce, Ca|8Al-8Mn-Ce and Ca|10Al-10Mn-5Ce.

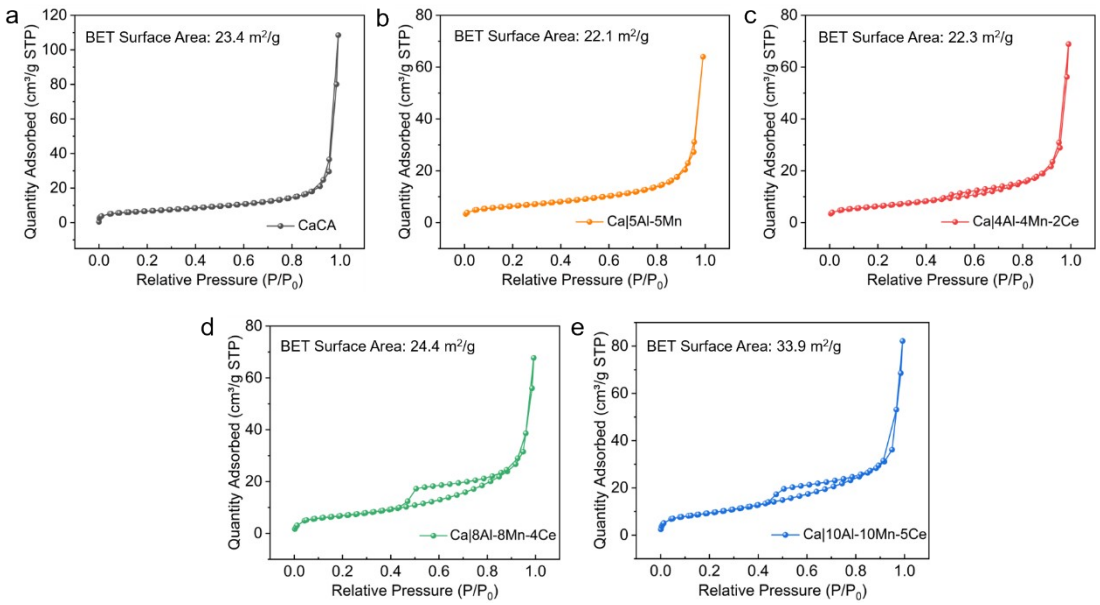

Figure S4. Nitrogen adsorption and desorption curves and BET surface area of (**a**) CaCA, (**b**) Ca|5Al-5Mn, (**c**) Ca|4Al-4Mn-2Ce, (**d**) Ca|8Al-8Mn-4Ce and (**e**) Ca|10Al-10Mn-5Ce.

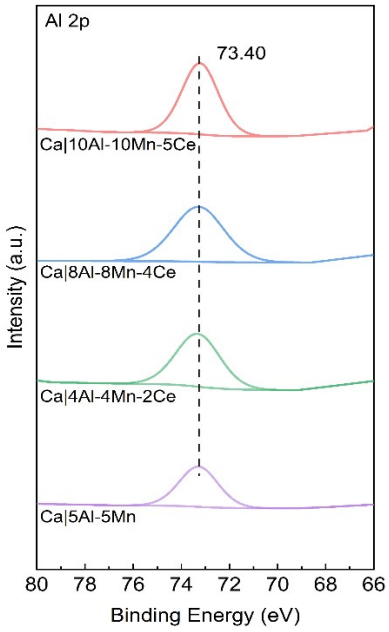

Figure S5 Al 2p XPS spectra of Al-doped CaO samples.

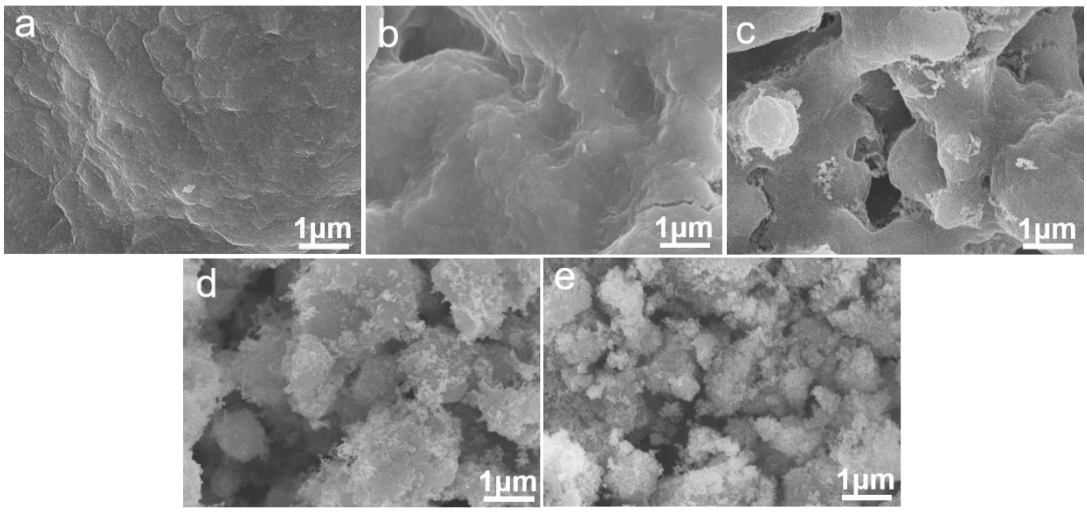

Figure S6. SEM images of Al/Mn/Ce composite CaO nanocarriers after 50 cycles (**a**) CaCA; (**b**) Ca|5Al-5Mn; (**c**) Ca|4Al-4Mn-2Ce; (**d**) Ca|8Al-8Mn-4Ce; (e) Ca|10Ald-10Mn-5Ce.

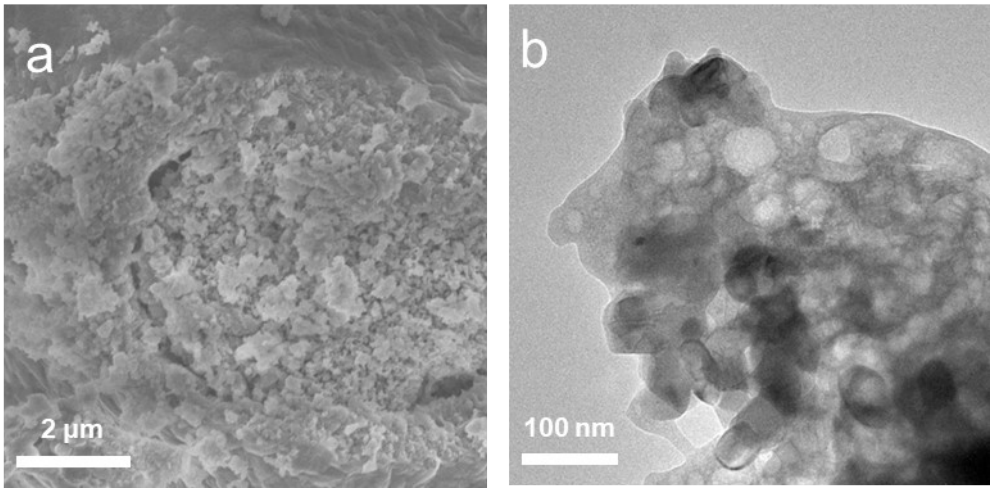

Figure S7. (**a**) SEM image of the Ca|8Al-8Mn-4Ce sample after 500 cycles. (**b**) TEM image of the Ca|10Al-10Mn-5Ce sample after 500 cycles

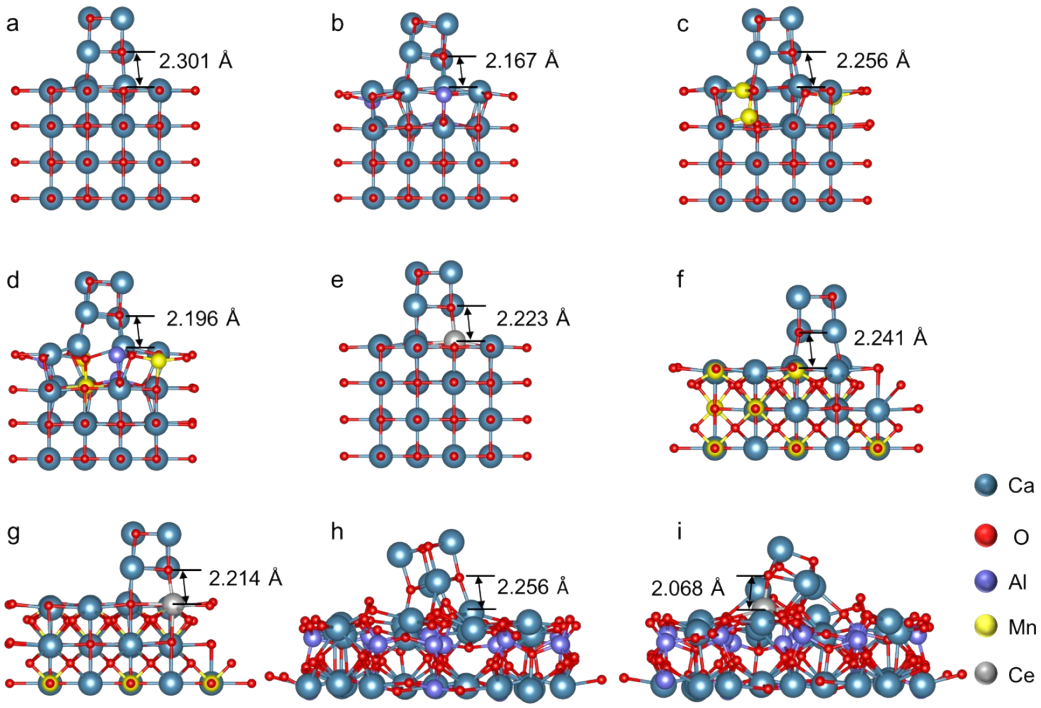

Figure S8. Optimized structures of (**a**) the CaO (100) with adsorbed CaO nanoclusters, (**b**) the Al/CaO(100) with adsorbed CaO nanoclusters, (**c**) the Mn/CaO(100) with adsorbed CaO nanoclusters, (**d**) the Al,Mn/CaO(100) with adsorbed CaO nanoclusters, (**e**) the Ce/CaO(100) with adsorbed CaO nanoclusters, (**f**) the $Ca_2MnO_4(110)$ with adsorbed CaO nanoclusters, (**g**) the $Ce/Ca_2MnO_4(110)$ with adsorbed CaO nanoclusters, (**h**) the $Ca_3Al_2O_6(011)$ with adsorbed CaO nanoclusters and (**i**) the $Ce/Ca_3Al_2O_6(011)$ with adsorbed CaO nanoclusters.

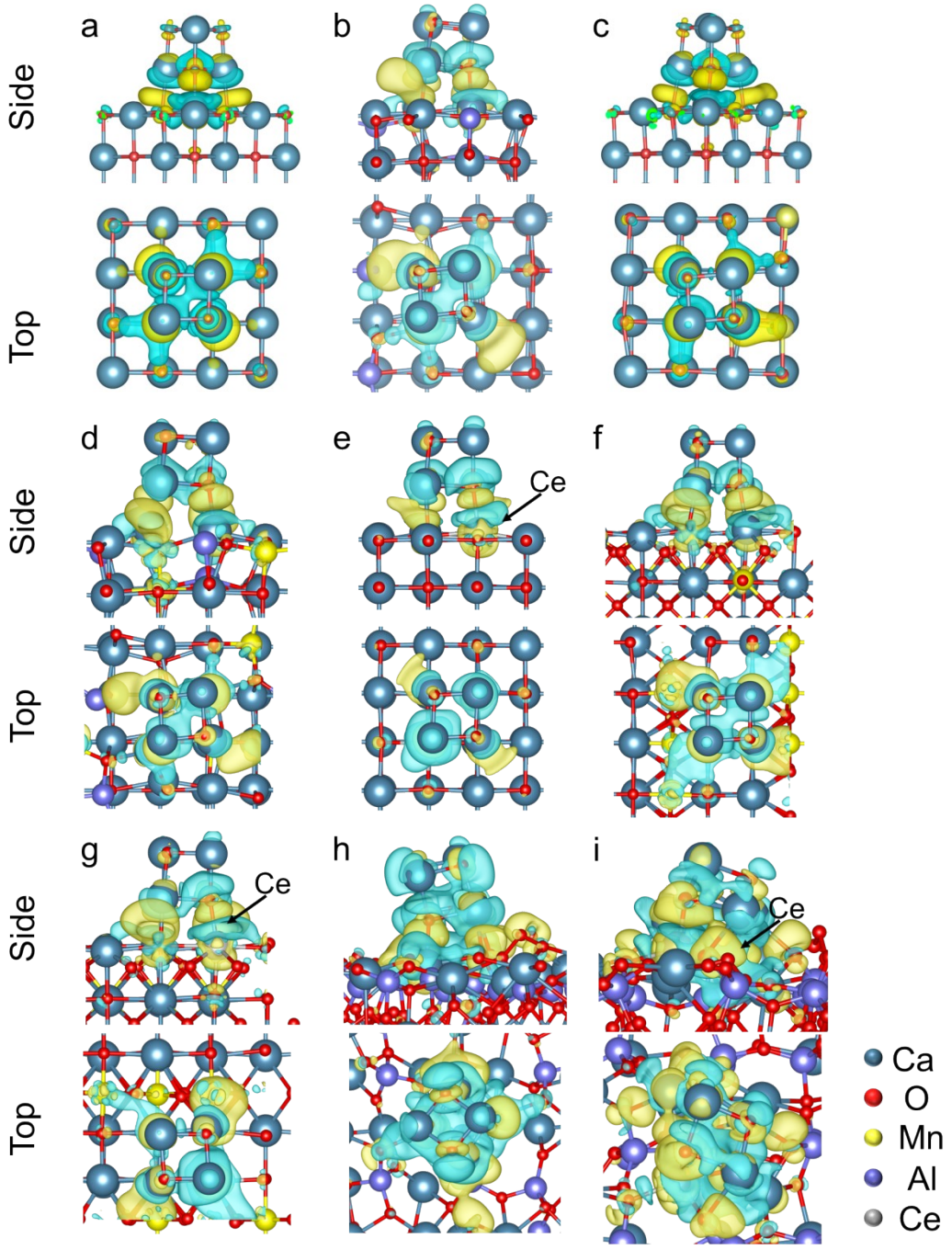

Figure S9. The differential charge density profile of (**a**) the CaO (100) with adsorbed CaO nanoclusters, (**b**) the Al/CaO(100) with adsorbed CaO nanoclusters, (**c**) the Mn/CaO(100) with adsorbed CaO nanoclusters, (**d**) the Al,Mn/CaO(100) with adsorbed CaO nanoclusters, (**e**) the Ce/CaO(100) with adsorbed CaO nanoclusters, (**f**) the Ca_2MnO_4(110) with adsorbed CaO nanoclusters, (**g**) the Ce/Ca_2MnO_4(110) with adsorbed CaO nanoclusters, (**h**) the $Ca_3Al_2O_6$(011) with adsorbed CaO nanoclusters and (**i**) the Ce/$Ca_3Al_2O_6$(011) with adsorbed CaO nanoclusters. Yellow and cyan represent electron accumulation and depletion region, respectively.

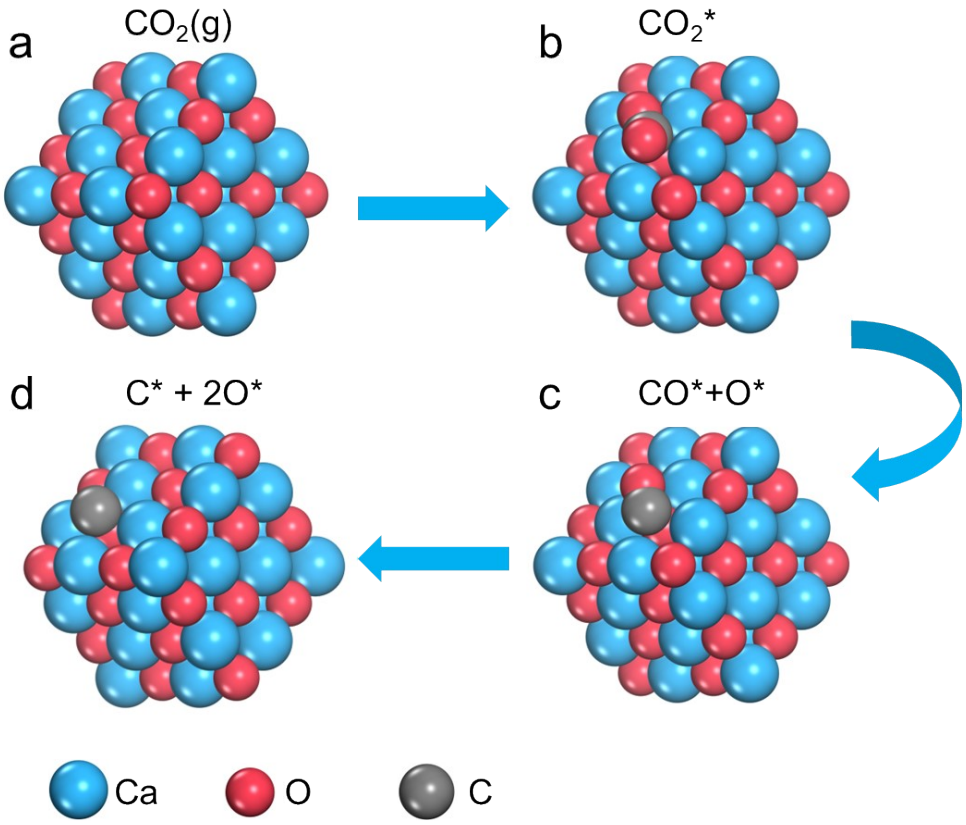

Figure S10. Optimized structures of reaction intermediates on CaO(100).

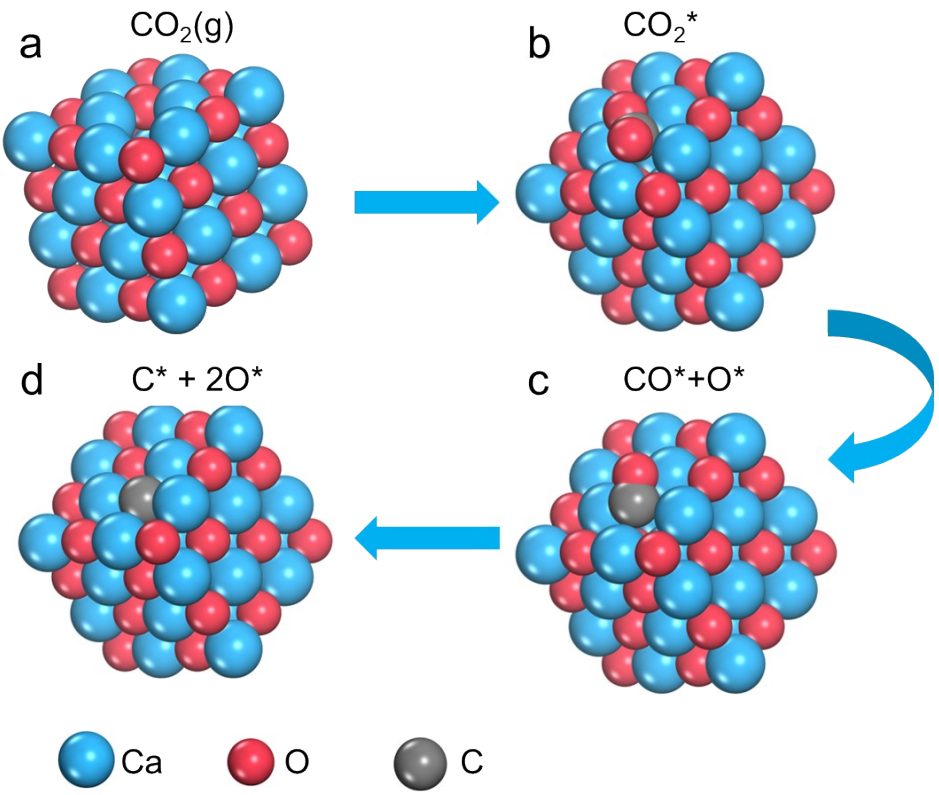

Figure S11. Optimized structures of reaction intermediates on CaO(100)/V (the V represents oxygen vacancy)

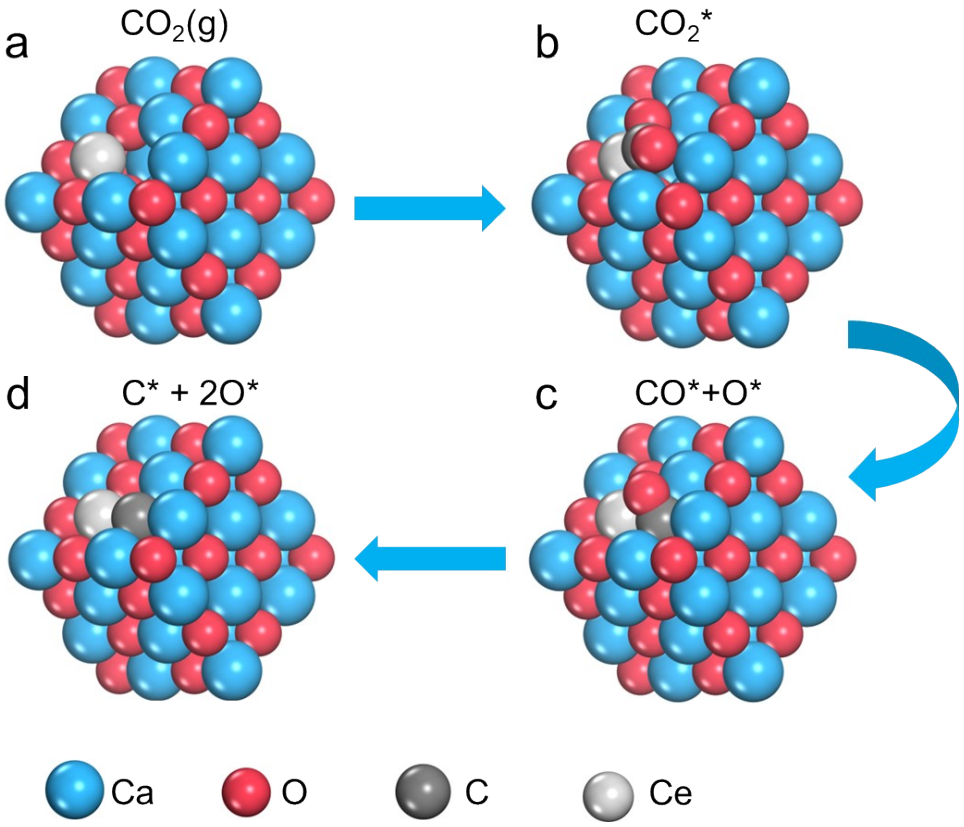

Figure S12. Optimized structures of reaction intermediates on Ce-CaO(100)/V (the V represents oxygen vacancy)

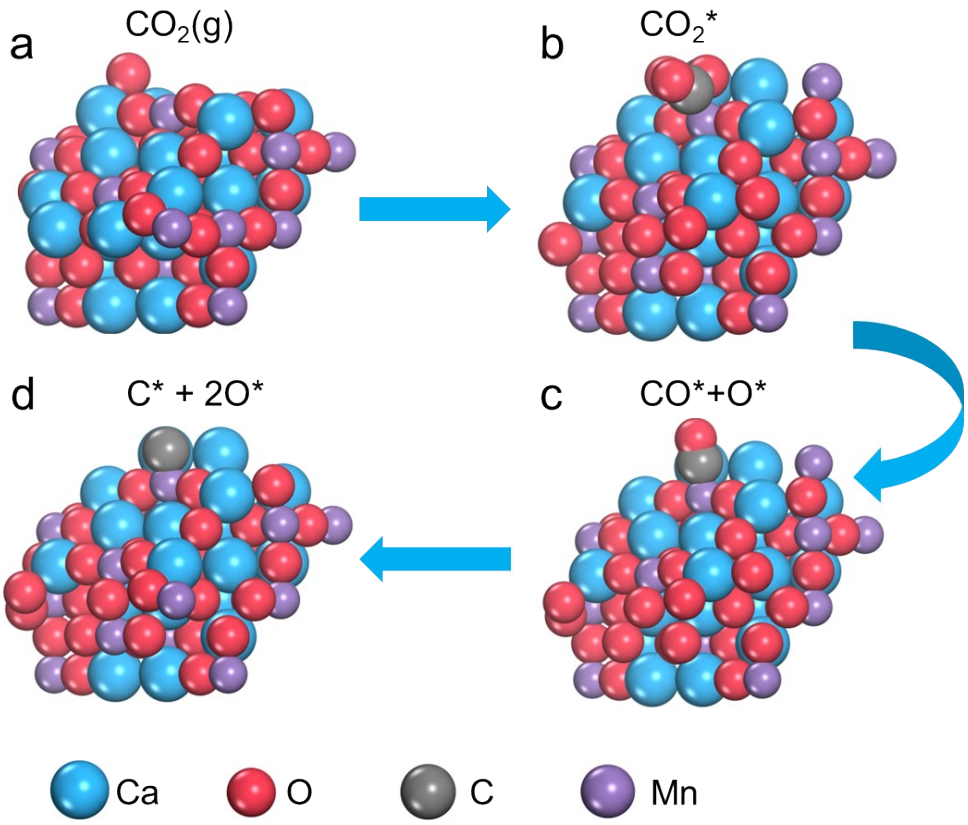

Figure S13. Optimized structures of reaction intermediates on Ca_2MnO_4(110)

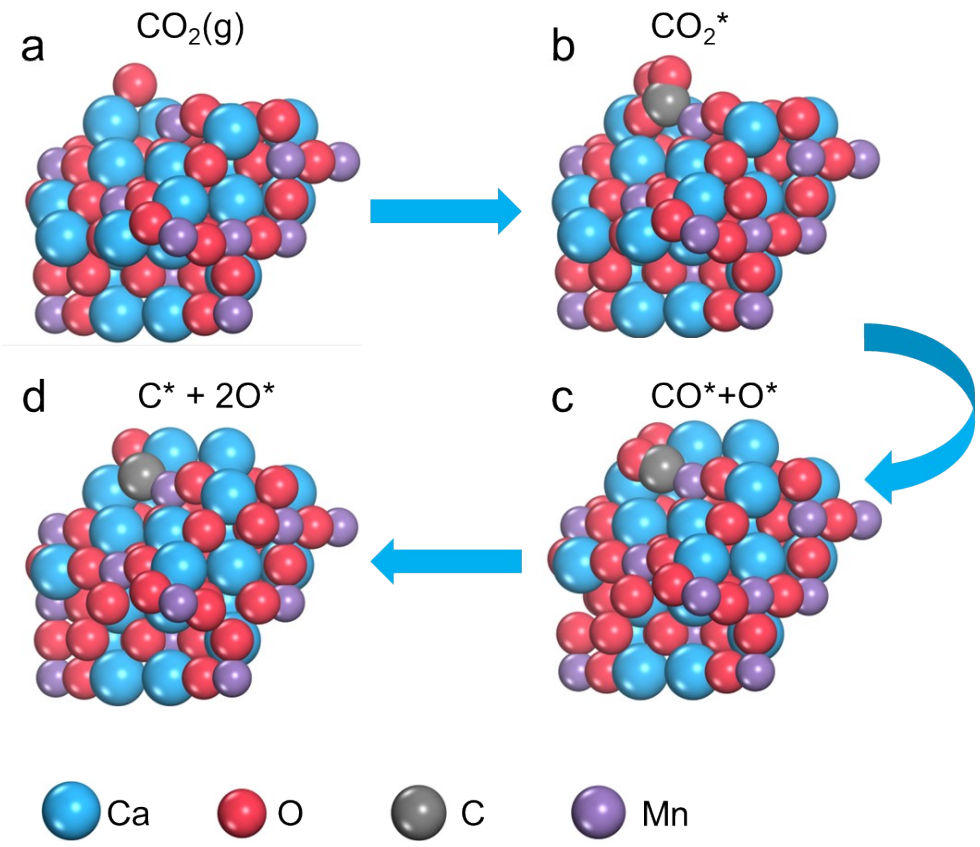

Figure S14. Optimized structures of reaction intermediates on Ca_2MnO_4(110)/V (the V represents oxygen vacancy)

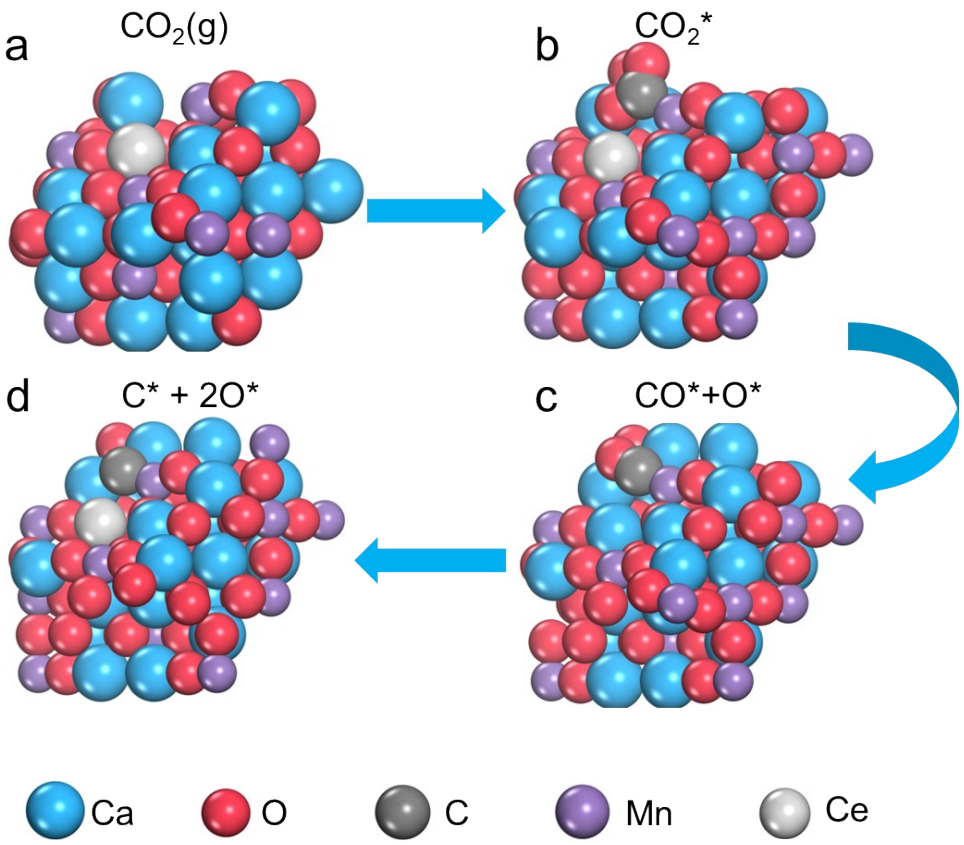

Figure S15. Optimized structures of reaction intermediates on Ce-Ca_2MnO_4(110)/V (the V represents oxygen vacancy)

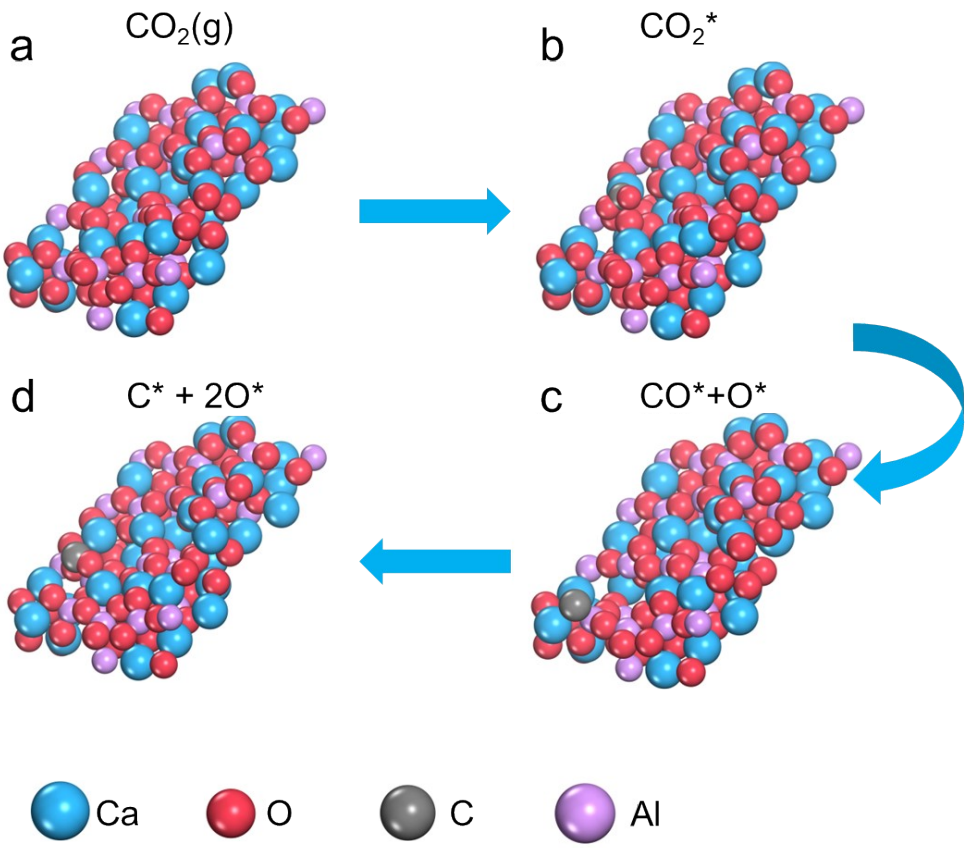

Figure S16. Optimized structures of reaction intermediates on $Ca_3Al_2O_6$(011).

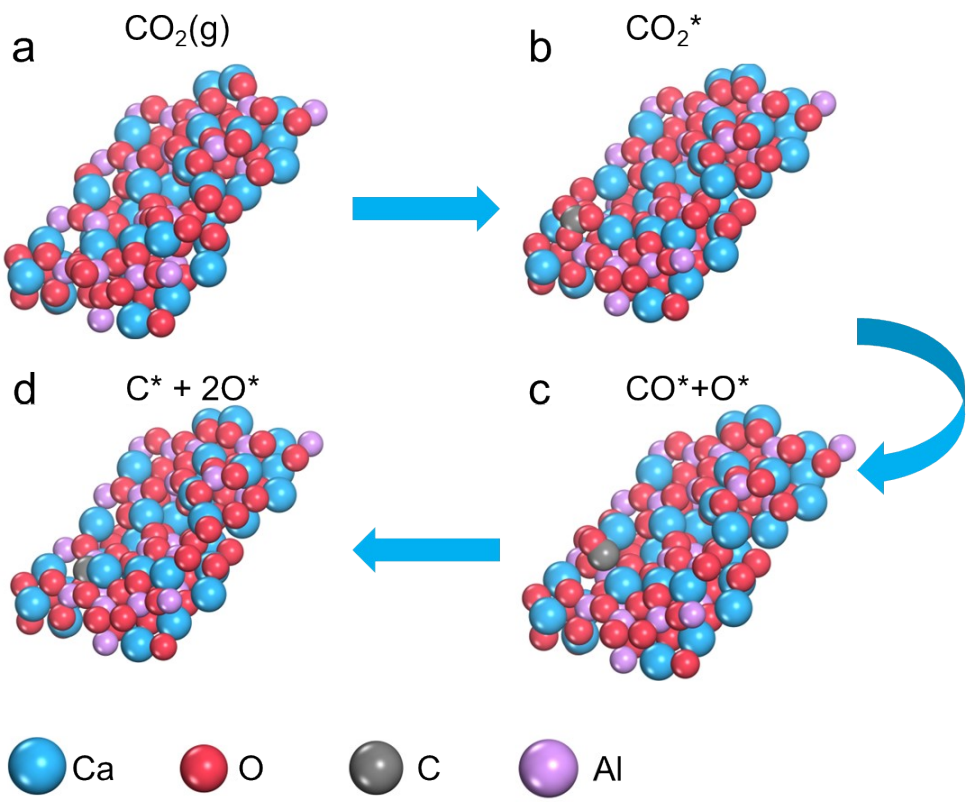

Figure S17. Optimized structures of reaction intermediates on $Ca_3Al_2O_6$(011)/V. (the V represents oxygen vacancy)

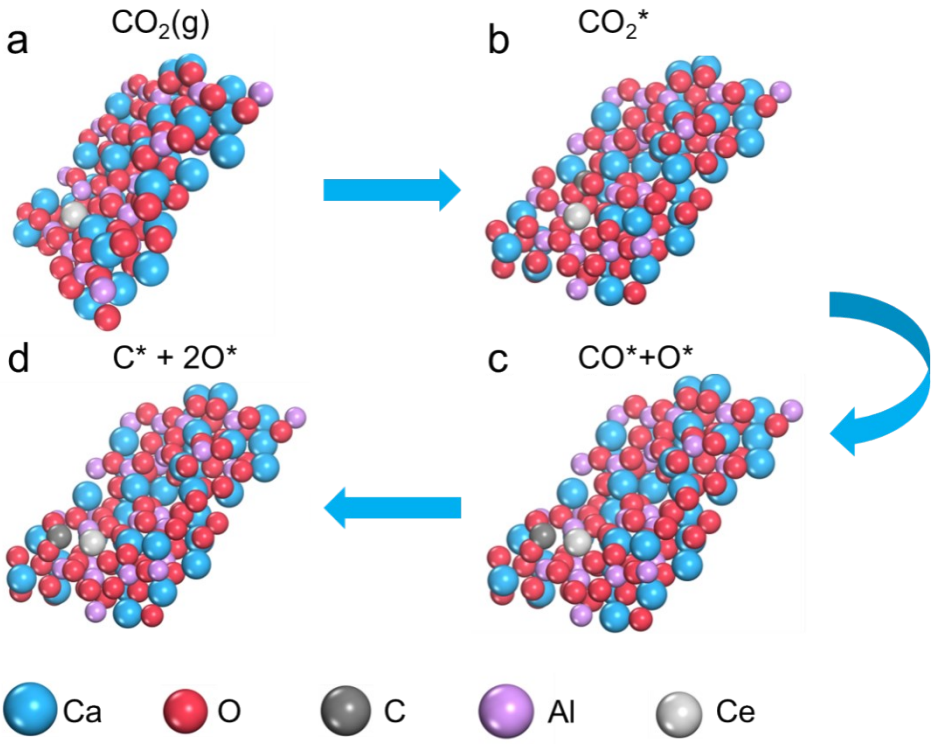

Figure S18. Optimized structures of reaction intermediates on Ce-$Ca_3Al_2O_6$(011)/V. (the V represents oxygen vacancy)

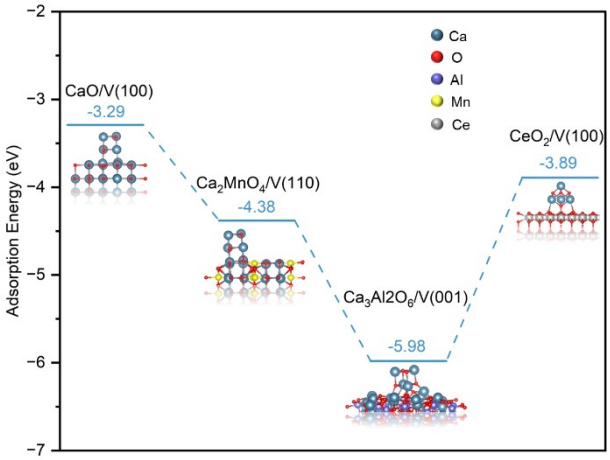

Figure S19. Adsorption energy of CaO nanoclusters on the CaO/V (100), Ca_2MnO_4/V (110) planes and $Ca_3Al_2O_6$/V (011) planes. The oxygen vacancies can enhance the adsorption energy and strengthen the interaction forces of the CaO/Ca|xAl-yMn-zCe sample, thereby improving the material stability.

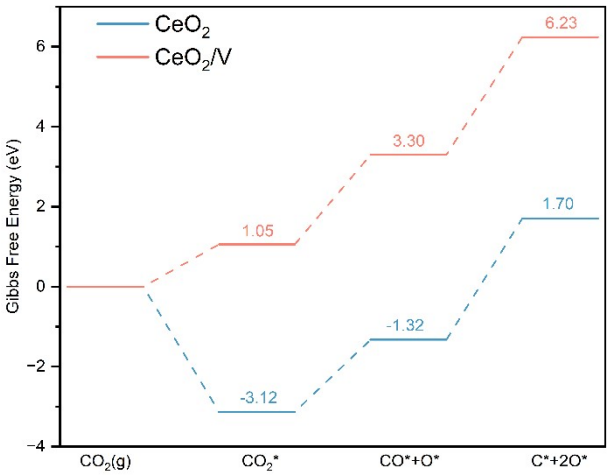

Figure S20. Gibbs free energy of the CO_2 splitting reaction over CeO_2 with oxygen vacancies. As expected, the presence of oxygen vacancies can significantly decrease the Gibbs free energy (*CO → *C + *O, rate-determining step) from +3.02 eV to +2.93 eV for CeO_2.

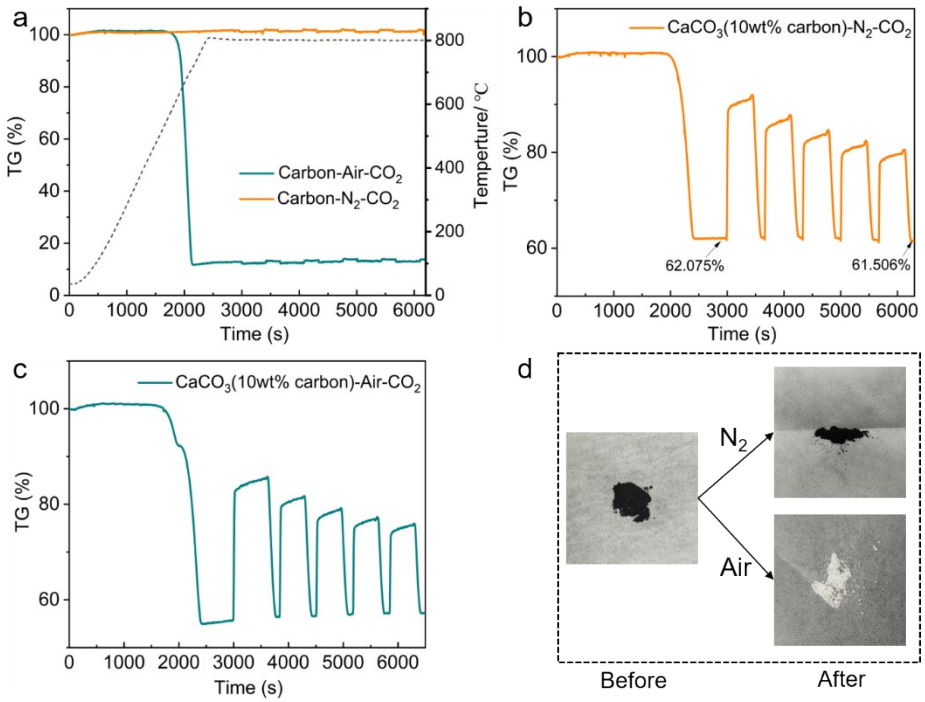

Figure S21(**a**) TG diagram of carbon black tested in N_2 and air calcination atmosphere for 5 cycles respectively; (**b**) TG diagram of 5 cycles of $CaCO_3$(10wt% carbon) under N_2 calcination atmosphere; (**c**) TG diagram of 5 cycles of $CaCO_3$(10wt% carbon) under air calcination atmosphere; (**d**) Macroscopic appearance of $CaCO_3$(10wt% carbon) before and after cycles under different calcining atmospheres.

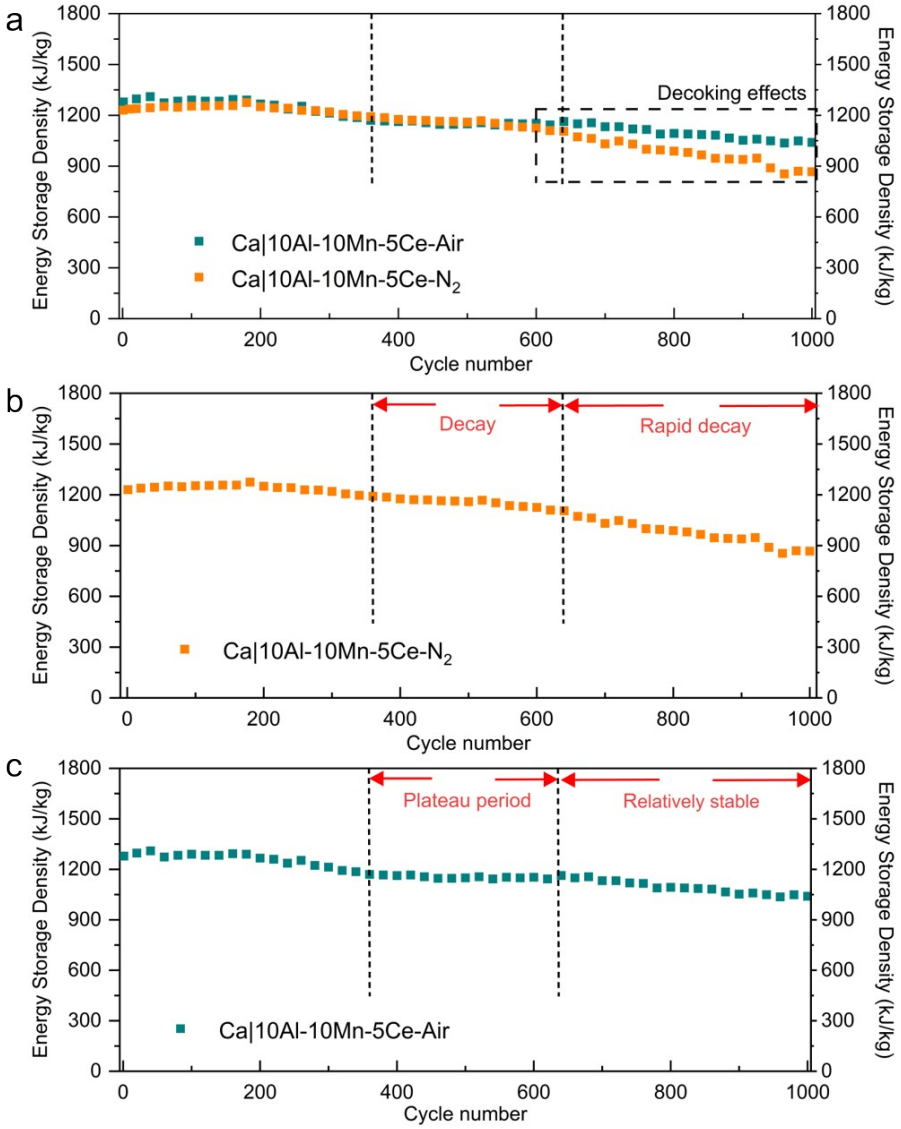

Figure S22 Stability of Ca|10Al-10Mn-5Ce after 1000 cycles under different calcination atmospheres, (**a**) N_2 or Air comparison, (**b**) N_2 atmosphere, (**c**) Air atmosphere.

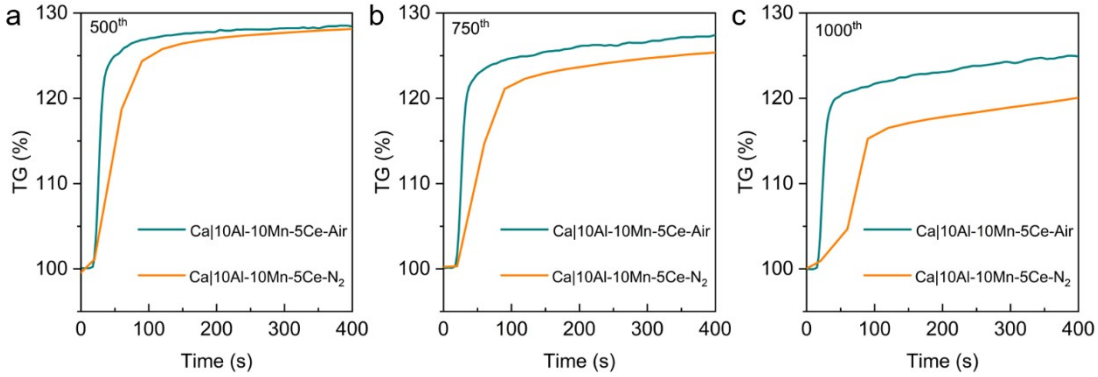

Figure S23. G curve of Ca|10Al-10Mn-5Ce carbonation under calcination atmosphere of Air and N_2, (**a**) 500th cycle; (**b**) 750th cycle; (**c**) 1000th cycle.

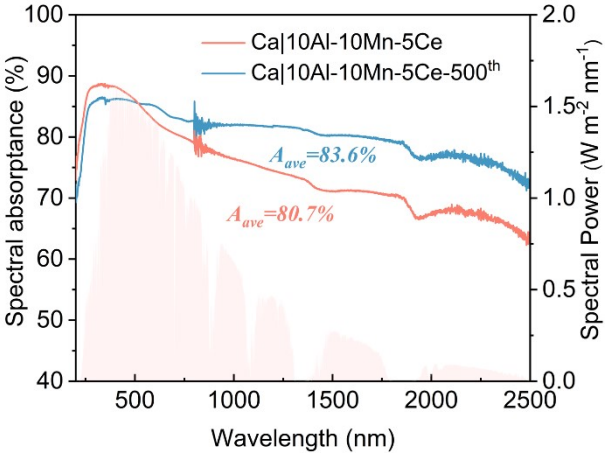

Figure S24. UV-Vis-NIR DRS spectra of Ca|10Al-10Mn-5Ce and Ca|10Al-10Mn-5Ce after 500 cycles. The average absorptance of Ca|10Al-10Mn-5Ce increased from 80.70% to 83.57% after 500 cycles, indicating that more dark species were generated on the surface of the materials after the cycling process, and amorphous carbon was formed.

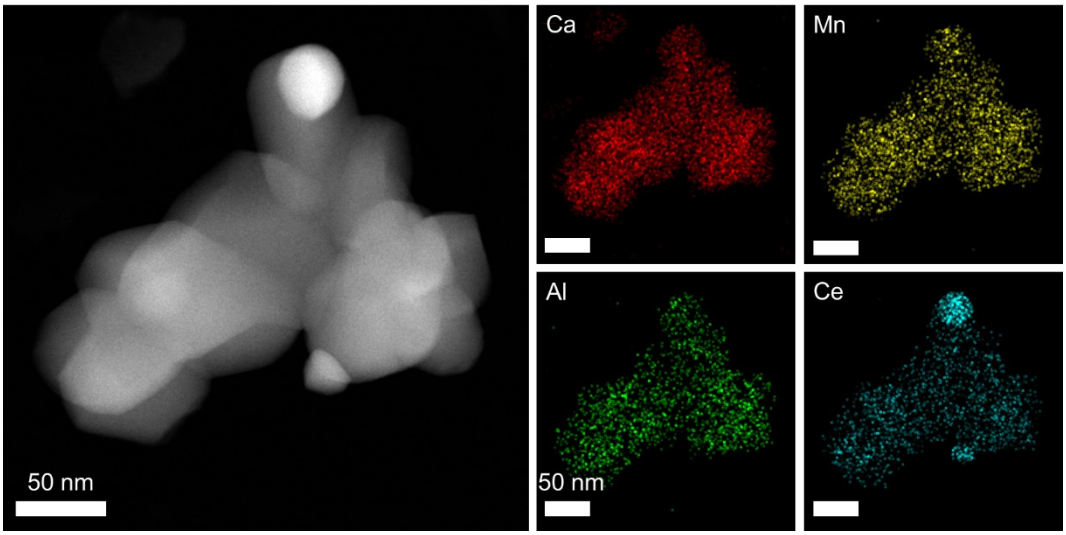

Figure S25. HAADF-STEM image, and EDX mapping images of Ca|10Al-10Mn-5Ce sample after 500 cycles under the oxidative atmosphere (Air-CO_2). The element distribution of the material in the 500 cycles is uniform, and no phase separation occurred. However, severe element phase separation was observed in the 1000 sample after 1000 cycles. Therefore, it indicates that the slow phase separation of $C_3aAl_2O_6$ and Ca_2MnO_4 is the cause of the deactivation.

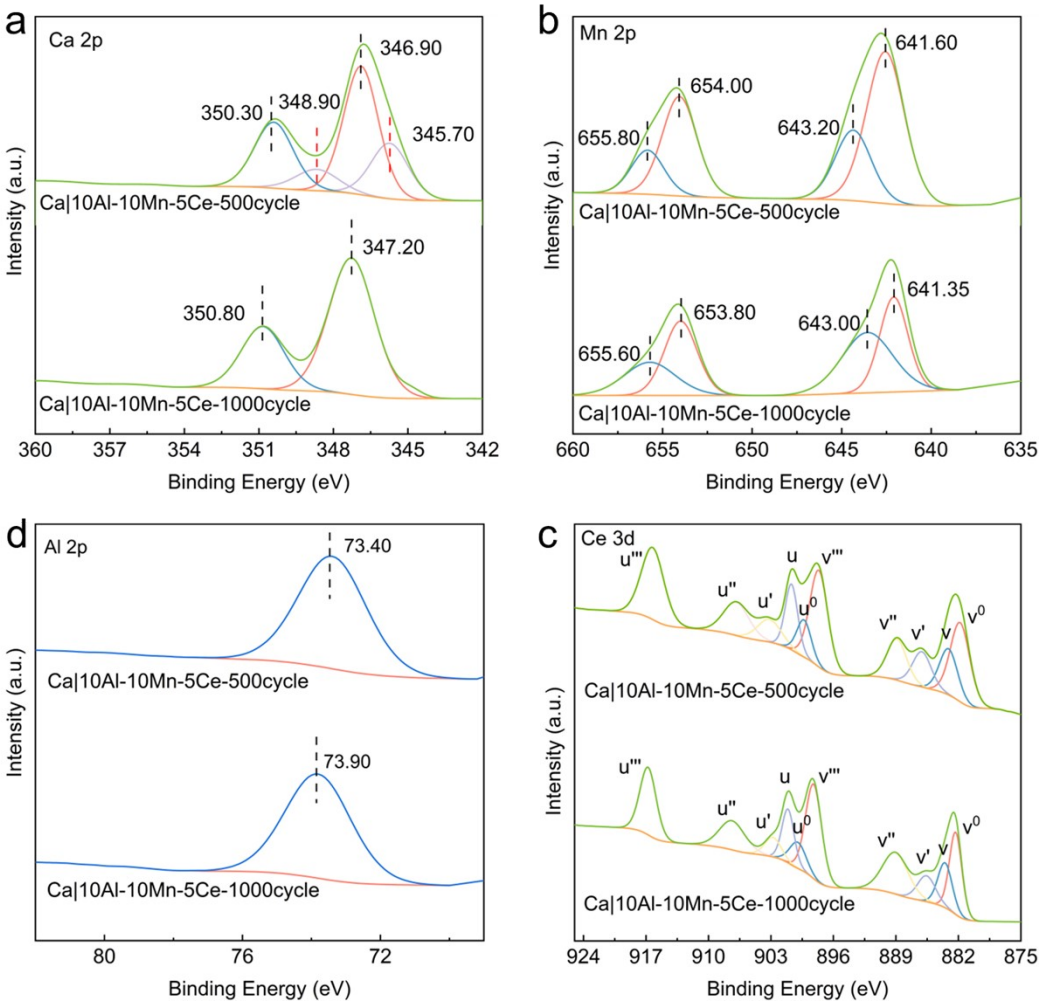

Figure 26. (**a**) Ca 2p, (**b**) Mn 2p, (**c**) Al 2p, and (**d**) Ce 3d XPS spectra of the Ca|10Al-10Mn-5Ce sample after cycles. It indicates that the Ce species did not change after the cycle, and the Ce^{3+}/Ce^{4+} ratio remained at around 30%.

Tabl S1 to 8

Table S1. The crystal cell parameters of as-synthesized metal doping CaO samples. (Space group: Fm-3m)

Samples	a[Å]	$d_{(200)}$ [Å]	V[Å^3]
CaCA	4.8252	2.4126	112.3430
Ca|5Al-5Mn	4.8287	2.4143	112.5876
Ca|4Al-4Mn-2Ce	4.8225	2.4112	112.1545
Ca|8Al-8Mn-4Ce	4.8224	2.4112	112.1475
Ca|10Al-10Mn-5Ce	4.8194	2.4097	111.9384
Ca|5Al-5Mn-5Ce	4.8200	2.4100	111.9802
Ca|8Al-5Mn-5Ce	4.8200	2.4100	111.9802
Ca|12Al-5Mn-5Ce	4.8277	2.4139	112.5177
Ca|5Al-8Mn-5Ce	4.8094	2.4047	111.2430
Ca|5Al-12Mn-5Ce	4.8179	2.4090	111.8339
Ca|5Al-5Mn-8Ce	4.8150	2.4075	111.6320
Ca|5Al-5Mn-12Ce	4.8422	2.4211	113.5346

Table S2. The BET surface area and pore volume of Al/Mn/Ce composite energy carriers.

Sample	BET Surface Area (m^2 g^{-1})	Pore volume of pores (cm^3 g^{-1})	Average pore diameter (nm)
CaCA	23.4	0.0465	8.0
Ca|5Al-5Mn	22.1	0.0434	7.8
Ca|4Al-4Mn-2Ce	22.3	0.0468	18.3
Ca||8Al-8Mn-4Ce	24.4	0.0503	11.8
Ca|10Al-10Mn-5Ce	33.9	0.0616	12.5

Table S3. The CaO grain size of different nanocarrier was calculated by Debye-Scherrer formula

Sample	Grain Size (nm)
CaCA	38.98
Ca|5Al-5Mn	40.39
Ca|4Al-4Mn-2Ce	41.09
Ca||8Al-8Mn-4Ce	39.80
Ca|10Al-10Mn-5Ce	36.63

Table S4. Binding energies of Ce 3d XPS peaks of Al/Mn/Ce composite energy carriers.

Sample	Binding energies of Ce 3d XPS peaks (eV)									
	v^0	v	v'	v''	v'''	u^0	u	u'	u''	u'''
Ca|4Al-4Mn-2Ce	881.7	883.1	885.9	888.8	897.5	899.2	900.6	903.2	906.8	916.1
Ca|8Al-8Mn-4Ce	881.8	883.0	885.9	888.8	897.7	899.2	900.6	903.3	906.9	916.2
Ca|10Al-10Mn-5Ce	881.8	883.2	886.1	888.9	897.6	899.3	900.7	903.2	906.9	916.1
Ca|10Al-10Mn-5Ce-500cycle	881.8	883.2	886.1	888.9	897.6	899.3	900.7	903.2	906.7	903.2
Ca|10Al-10Mn-5Ce-1000cycle	881.8	883.1	886.1	888.9	897.6	899.3	900.7	903.2	903.2	903.2

Table S5. Ce^{3+} relative amount (%) of Al/Mn/Ce co-doping energy carriers.

Sample	relative amount (%)
Ca|4Al-4Mn-2Ce	28.2
Ca|8Al-8Mn-4Ce	29.1
Ca|10Al-10Mn-5Ce	31.6
Ca|10Al-10Mn-5Ce-500cycle	31.9
Ca|10Al-10Mn-5Ce-10cycle	30.7

Table S6. Representative works on Ca-based thermochemical energy storage.

Samples	Total energy storage density [kJ kg^{-1}][a]	Initial energy storage density [kJ kg^{-1}]	Cycle number	Energy storage density after cycle [kJ kg^{-1}]	Attenuation	Conditions (carbonation/ calcination)
This work Ca|10Al-10Mn-5Ce	1.13×10^6	1230.0	1000	1039.6	15.5%	800 ℃, 7.5 min/800 ℃, 6 min
This work Ca|8Al-8Mn-4Ce						800 ℃, 7.5 min/800 ℃, 6 min
This work Ca|4Al-4Mn-2Ce						800 ℃, 7.5 min/800 ℃, 6 min
Mg/CaO[11]	3.94×10^4	2034.0	30	1907	6.3%	650 ℃, 20 min/900 ℃, 5 min
Al/CaO[12]	5.62×10^4	2002	30	1748	12.7%	650 ℃, 20 min/900 ℃, 10 min
Na/CaO[13]	8.18×10^4	2161	50	1112	48.5%	650 ℃, 20 min/800 ℃, 10 min
Ti, Ni/CaO[14]	2.56×10^4	1296	20	1267	2.2%	750 ℃, 10 min/850 ℃, 5 min
Mn, Zr/CaCO3[9]	2.07×10^4	1706	125	1604	6.0%	800 ℃, 7 min/800 ℃, 4 min
Mn, Fe/CaO[15]	5.96×10^4	636	100	556	12.5%	750 ℃, 60 min/750 ℃, 60 min
Ce, La, Nd, Yb, Zr/CaO[16]	1.83×10^4	1748	20	1653	5.4%	650 ℃, 30 min/850 ℃, 5 min
Mn, Mg/CaO[17]	1.49×10^4	1520	100	1460	4.0%	800 ℃, 10 min/800 ℃, 8 min

Ni, Zr/CaO[18]	1.23×10^4	2100	60	2000	4.8%	850 ℃, 10 min/750 ℃, 15 min
Mn, Ce/CaO[19]	4.86×10^4	2480	20	2385	3.8%	850 ℃, 10 min/850 ℃, 10 min
SiO_2/CaO[20]	9.30×10^4	2542	50	1176	53.7%	850 ℃, 35 min/650 ℃, 40 min

[a] The formula for total energy storage density is $\sum_{i}^{n} En$, where n represents the number of cycles and En represents the energy storage density for each cycle. To unify the standards, the energy storage density of all materials decreases linearly.

Table S7. Carbon content of Ca|10Al-10Mn-5Ce before and after 500 cycles.

sample	C (%)
Ca|10Al-10Mn-5Ce	0.84
Ca|10Al-10Mn-5Ce -500th	1.31

Table S8. Adsorption energy of CaO clusters on different substrates.

Name	The adsorption energy (eV)
CaO(100)	-2.92
Mn/CaO(100)	-3.78
Al/CaO(100)	-3.94
AlMn/CaO(100)	-3.69
Ce/CaO(100)	-3.73
Ca_2MnO_4(110)	-4.18
Ce/Ca_2MnO_4(110)	-4.47
$Ca_3Al_2O_6$(011)	-5.76
Ce/$Ca_3Al_2O_6$(011)	-6.48

References:

1. T. Wu, P. Zhang, Y. Wei, J. Xiong, D. Han, T. Li, Y. Yang, Z. Zhao and J. Liu, *ACS Catalysis*, 2024, **14**, 1882-1902.
2. G. Kresse, J. Furthmüller, *Phys. Commun*, 1996, **6**, 15-50.
3. G. Kresse, D. Joubert, Phys. Rev B, 1999, **59**, 1758-1775.
4. J. P. Perdew, K. Burke, Ernzerhof, M. Rev. Lett, 1996, **77**, 3865-3868,.
5. S. Grimme, S. Ehrlich and L. Goerigk, *Journal of Computational Chemistry*, 2011, **32**, 1456-1465.
6. D. J. Chadi and M. L. Cohen, Physical Review B, 1973, **8**, 5747-5753.
7. V. Wang, N. Xu, J.-C. Liu, G. Tang and W.-T. Geng, *Computer Physics Communications*, 2021, **267**, 108033.
8. K. Momma and F. Izumi, *Journal of Applied Crystallography*, 2011, **44**, 1272-1276.
9. H. Li, J. Lin, J. Wu, J. Wang, P. Wang, G. Kang, S. Huang, M. Fu, J. Wei, Z. Ding and J. Long, *Advanced Science*, 2024, **12**, 2412082.
10. J. Zhang, J. Ma, T. S. Choksi, D. Zhou, S. Han, Y.-F. Liao, H. B. Yang, D. Liu, Z. Zeng, W. Liu, X. Sun, T. Zhang and B. Liu, *Journal of the American Chemical Society*, 2022, **144**, 2255-2263.
11. M. A. Naeem, A. Armutlulu, Q. Imtiaz, F. Donat, R. Schäublin, A. Kierzkowska and C. R. Müller, *Nature Communications*, 2018, **9**, 2408.
12. A. Armutlulu, M. A. Naeem, H. J. Liu, S. M. Kim, A. Kierzkowska, A. Fedorov and C. R. Müller, *Advanced Materials*, 2017, **29**, 1702896.
13. M. Krödel, L. Abduly, M. Nadjafi, A. Kierzkowska, A. Yakimov, A. H. Bork, F. Donat, C. Copéret, P. M. Abdala and C. R. Müller, *Advanced Functional Materials*, 2023, **33**, 2302916.
14. Guo SJ, Tian XK, Yan J, Ju SH, Zhao CY. Performance enhancement mechanisms of calcium-based thermochemical energy storage compounds: insights from first-principles and experimental investigations. *J. Mater. Chem. A*, 2024, **12**, 14129-14147.

15. Desage L, Humphries TD, Paskevicius M, Buckley CE, *J. Mater. Chem. A*, 2024, **12**, 14721-14733.

16. Y. Long, Q. Gu, C. Wang, X. Zhang, H. Liu, L. Liu and Z. Zhou, *Small*, 2024, **20**, 2406165.

17. H. Liu, Y. Li and J. Wei, *Chemical Engineering Journal*, 2024, **480**, 147892.

18. Z. Li, L. Li, J. Liu, Q. Niu, Z. Fang, J. Li, K. Li, Q. Lu, *Chem. Eng. J*, 2025, **523**, 168897.

19. Y. Zhang, Y. Fang, Z. Chu, Z. He, J. Zhao, K Han, Y Li, *J. Energy Chem*, 2025, **107**, 170-182

20. C.-C. Li, U.-T. Wu and H.-P. Lin, *J. Mater. Chem. A*, 2014, **2**, 8252-8257.